Corrosion Science 173 (2020) 108749

Contents lists available at ScienceDirect

Corrosion Science

journal homepage: www.elsevier.com/locate/corsci

The origin of passivity in aluminum-manganese solid solutions[★]

Jia Chen[a,1], Jianwei Xiao[b,1], Jonathan Poplawsky[c], F. Marc Michel[d], Chuang Deng[b,*], Wenjun Cai[a,*]

[a] Department of Materials Science and Engineering, Virginia Polytechnic Institute and State University, Virginia, 24061, United States
[b] Department of Mechanical Engineering, University of Manitoba, Winnipeg, MB R3T 5V6, Canada
[c] The Center for Nanophase Materials Sciences, Oak Ridge National Laboratory, Tennessee, 37831, United States
[d] Department of Geosciences, Virginia Polytechnic Institute and State University, Virginia, 24061, United States

ARTICLE INFO

Keywords:
Al alloys
Corrosion
Atom probe tomography
X-ray photoelectron spectroscopy
Atomistic simulation

ABSTRACT

The effects of manganese on the aqueous corrosion of aluminum-manganese alloys were investigated by experiments and atomistic simulations. Electrochemical measurements, x-ray photoelectron spectroscopy, and atom probe tomography analysis indicate that manganese addition enhanced the corrosion resistance of aluminum without participating in the surface oxidation. The selective dissolution of manganese was believed to increase the free volume at the metal/oxide interface to facilitate the formation of a denser, thinner oxide layer with closer to stoichiometry composition. Atomistic simulations showed that the oxide layer compactness increased, and defect density decreased with increasing free volume content in Al, resulting in enhanced barrier characteristics.

1. Introduction

The design of strong and corrosion-resistant alloys, especially those containing lightweight elements such as Al are challenged by the trade-off between strength and corrosion resistance. Solute tends to have small equilibrium solubility limit in Al due to their relatively large negative enthalpy of mixing with Al [1]. As a result, extensive precipitates are often formed to strengthen Al alloys, which compromises corrosion resistance due to the microgalvanic coupling with the metal matrix (with the matrix serving as the local anode) [2,3]. The presence of precipitates also degrade the passive film's resistance to localized corrosion due to the thickness incompatibility between the precipitates and Al matrix [4]. Such design challenge is also complicated by the fact that a fundamental understanding of the far-from-equilibrium structure, property, and formation mechanism of the passive layer of Al alloys is still lacking, where unusual combinations of structure and chemical composition are a general phenomenon, resulting from different diffusion and transport rates of the constituting elements, selective dissolution or oxidation, and the moving oxidation front, as pointed out recently by Yu et al. in the 'nonequilibrium solute capture' theory [5].

An outstanding question is how to select the appropriate alloying elements and composition to obtain a naturally occurring, protective, and mechanically robust oxide layer on the surface of Al yet minimizing the strength-corrosion resistance trade-off. In the present work, we evaluate an intriguing hypothesis, that the corrosion resistance of Al alloys could be enhanced by increasing the content of a non-passive element (Mn) in solid solution; such non-passive element is selectively dissolved at the surface to enhance surface activity of Al and facilitate the formation of a more compact (i.e. higher density), thinner, yet protective surface oxide layer with closer to stoichiometry composition than those on pure Al or dilute Al-Mn alloys. Here, solid solution is chosen as an 'electrochemically benign' strengthening mechanism that does not introduce measurable chemical heterogeneity [6–9]. Thanks to the fast effective quenching rate during non-equilibrium processes such as physical vapor deposition, metastable solid solutions of Al-based binary and ternary thin films have been prepared and their corrosion properties studied extensively [6–12]. Previous studies show that the effects of alloying additions on the pitting corrosion resistance of such

---

[*] Corresponding authors.
E-mail addresses: Chuang.Deng@umanitoba.ca (C. Deng), caiw@vt.edu (W. Cai).

[1] co-first author.

https://doi.org/10.1016/j.corsci.2020.108749
Received 19 February 2020; Received in revised form 17 May 2020; Accepted 17 May 2020

Al-based solid solutions are complex [12,13]. Small quantities of Sn, In, Hg, Ga, and Zn are found to be detrimental to Al corrosion, as they reduce the passive potential region and shift the corrosion and pitting potentials in the negative direction [14]. Thus, these alloying elements lead to high anodic current density and uniform active surface corrosion. Other alloying elements such as Cu, Mo, Mn, W, Nb, Cr, Ta, V, and Zr improve corrosion resistance and decrease pitting susceptibility of Al by increasing the overpotential for anodic dissolution and decreasing metastable pit initiation and growth rates [6,15]. Specifically, in terms of the roles of Mn addition, the pitting resistance of Al was improved by ~ 350–500 mV and corrosion current density reduced by ~ 2–10 times when alloyed with up to ~ 30 at.% Mn compared to pure Al [10,11,16]. It should also be noted that with increasing Mn content, the microstructure of the alloy experiences a transition from nanocrystalline to complete amorphous structure at high Mn content [11,16–18]. However, as reported previously [11], the pitting potential increases monotonically with Mn content up to ~ 20 at.%, regardless of its crystallinity. It is also interesting to note that when Mn content further increases to above ~ 40 at.%, a reduction of pitting potential was also reported [16]. Several explanations have been proposed to elaborate the roles of Mn on the corrosion behavior of Al. It was suggested that its influence on the composition of the passive layer is small, rather its effects on enhancing the corrosion resistance of Al has been attributed to its influence on the pH of zero charge of the passive film, the solubility of dissolved species in the pit solution, enrichment of the solute species at the active surface in a pit, and ennobling the pit dissolution kinetics [10,16,19–21]. It was argued that when Mn is added, higher potentials are needed to achieve the high current densities necessary for stable pit growth compared to pure Al, which leads to higher pitting potential [19,22]. Limited studies have been performed to identify the structural origin of such corrosion behavior. For example, Crossland et al. [23] studied the structure of barrier-type anodic films (~ 132 nm thick) of Al-2.5 at.% Mn and Al-16 at. % Mn in ammonium pentaborate, sodium hydroxide, and sulphuric acid electrolytes. They found that under the anodization voltage of 60 and 100 V, the faster migration of Mn species than Al leads to the formation of a bilayered anodic film in pentaborate and hydroxide solutions (pH > 7), with the inner film enriched in Al_2O_3 and MnO, and an outer layer of primarily Mn_2O_3. However, in sulphuric acid (pH < 7), no outer Mn-rich layer was observed. On the other hand, Zhang et al. [21] showed that the passive film of Al-23.7 wt.% Mn at open circuit potential contains mainly alumina and hydrated alumina during long term (2808 h) immersion in 3.5 wt.% NaCl aqueous solution, while no prominent Mn oxide was detected, similar to those reported by Moffat et al. [20].

The lack of fundamental understanding of the atomistic structure, composition, and chemical state of the passive layer and their formation mechanism, which is difficult to characterize due to its thinness and delicate structure, has greatly hindered our understanding of the specific roles Mn play on the corrosion behavior of Al. Such challenge is coupled with a lack of understanding of the defect type and density in the passive layer, which often dominate the charge and mass transfer events that govern both the oxide growth and metal dissolution kinetics. For example, the argument on the pit dissolution kinetics cannot explain why the pitting potential of Al-Mn starts to decrease when Mn% is above ~ 40 at.%. The present work aims to combine atomistic surface characterization (e.g. 3D atom probe tomography) and computer simulation (molecular dynamics) to understand the roles of Mn addition on the structure, chemistry, and protectiveness of the surface oxide layer of Al-Mn alloys and its barrier characteristics. Atom probe tomography (APT) is the only technique so far capable of producing 3D compositional reconstructions with sub-nanometer-scale resolution and ~10 ppm sensitivity, and has only recently been applied to corrosion science [24–26]. Specifically, we studied the aqueous corrosion of a concentrated binary alloy of Al-20 at.% Mn, commercial Al-Mn alloy (Al 3003), and high purity Al. Finally, a rationalization of the origin of passivity in Al-based solid solution is proposed based on the experimental and simulation results. The obtained understanding could shed light on the design of new corrosion-resistant concentrated alloys such as multi-principle elements alloys, high entropy alloys, and metallic glasses.

2. Experimental procedure

Al-Mn thin films with a nominal composition of 20.3 at.% Mn were prepared by direct current (DC) magnetron sputtering on (100) silicon (Si) wafers. Sputtering was operated inside a vacuum chamber (PVD 75, Kurt J. Lesker, Pennsylvania, USA), applying 200 W power for the Al (99.99 %, Kurt J. Lesker, Pennsylvania, USA) target and 38 W for the Mn target (99.95 %, Kurt J. Lesker, Pennsylvania, USA) under 5.9×10^{-3} Torr argon atmosphere (99.99 %). Prior to the deposition, Si wafers were etched with 1:20 hydrofluoric acid water solution to remove the natural oxidation layer. The thickness of the thin film was ~ 1.2 μm, measured by a contact profilometer (DektakXT, Bruker, Massachusetts, USA). The chemical composition of samples was characterized by energy-dispersive X-ray spectroscopy (EDS, Quantax, Bruker, Massachusetts, USA) in a scanning electron microscopy (SEM, Quanta 600 FEG, FEI, Oregon, USA) under 10 keV.

Electrochemical measurements were performed on as-deposited and anodized Al-20 at.% Mn thin films (hereafter referred as AM20 and a-AM20 respectively), Al 3003 (Metal Supermarkets, Florida, USA), and high purity Al (99.99 %, Alfa Aesar, Massachusetts, USA) with an effective exposed area of ~ 1 cm^2. The chemical composition (in mass fraction) of Al 3003 is 1.14 % Mn, 0.15 % Cu, 0.60 % Fe, 0.10 % Si, and balanced Al. A potentiostat/galvanostat/zero resistance ammeter (Gamry model 600, Pennsylvania, USA) was used for all electrochemical experiments in a three-electrode setup, where the sample, a mixed metal oxide coated titanium mesh, and a silver-silver chloride electrode with 1 M KCl internal solution was used as the working, counter, and reference electrode respectively. Naturally aerated 0.6 M NaCl aqueous solution with pH ≈ 6.4 at 25 ± 2 °C was used as the electrolyte in all experiments. The a-AM20 sample was prepared by anodic polarization of AM20 at a constant potential of 200 mV above the open circuit potential (E_{ocp}) at 15 °C for 2000 s. This anodizing potential was chosen within the passive region where the current density is largely independent of potential. The lower temperature (than room temperature) is chosen to suppress the generation of joule heating [27]. The enhanced protectiveness of this passive layer on a-AM20 is confirmed by the current evolution during anodizing, as shown in Fig. 1, where the current density decreased from ~ 7.75×10^{-8} A/cm^2 to 3.68×10^{-8} A/cm^2 after 2,000 s. Potentiodynamic polarization (PD) tests were performed with a scan rate of 0.167 mV/s for 1.5 h after stabilizing at E_{ocp} for 300 s, starting at a potential of −150 mV below

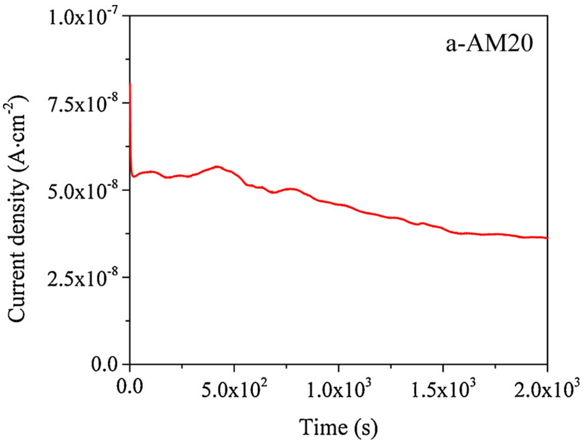

Fig. 1. Current evolution during potentiostatic anodizing of AM-20 in 0.6 M NaCl solution at 15 °C.

E_{ocp}. Electrochemical impedance spectroscopy (EIS) analysis was performed after 300 s stabilization at E_{ocp}, with 10 mV_{rms} sinusoidal potential excitation, 100 kHz to 10 mHz frequency, and 5 points per decade. Note the time allowed for E_{ocp} stabilization (300 s) was determined by measuring the time evolution of E_{ocp} until no significant fluctuations of potential was recorded, as confirmed by E_{ocp} measurements over a longer period of 1800 s on selected samples. The obtained data was then fitted by the equivalent circuit (EC) model using Gamry E-chem software. Mott-Schottky (M–S) test was performed to analyze the electronic properties of passive layer on all samples at a frequency of 1000 Hz and scan rate of 10 mV/s, after immersion at E_{ocp} for 600 s. The potential scan range of pure Al and Al 3003 were from -1.0 V to -0.7 V vs. their respective E_{ocp} while that of AM20 and a-AM20 were from -1.0 V to -0.1 V vs. their respective E_{ocp}.

X-ray diffraction (XRD) measurements of pure Al and Al 3003 was performed using PANalytical X'pert PRO MRD at 0.01° step size, 2.5 s scan step time, using Cu Kα under 45 kV and 40 mA. Grazing incidence XRD (GI-XRD) of AM20 and a-AM20 were performed using PANalytical Empyrean Nano Edition with a grazing incidence angle of 0.9149°, 0.02° step size and 10 s scan step. The X-ray photoelectron spectroscopy (XPS, PHI Quantera SXM, USA) characterization was operated under an ultra-high-vacuum system with 10^{-9} Torr base pressure. On each sample, a monochromatic Al Kα X-ray source with a beam diameter of 100 μm and an angle of 45° source analyzer was applied to measure the sputter depth profiles. Pre-sputtering was applied for 15 s using 1 kV ion beam directly on the sample surface to remove any potential carbon contamination. The sputter depth profiles were obtained using $1-3$ kV argon ions on an area of ~ 2×2 mm^2 using a number of sweeps, step sizes and pass energy, as shown in Table 1. The estimated instrumental resolution is ~ 0.39 eV for O 1s spectra, 1.0 eV for Al 2p spectra and ~ 2.1 eV for Mn 2p spectra. C 1s at 285 eV was used to calibrate the spectrum prior to data analysis of each element. MultiPak analysis software was used to perform the spectral deconvolution after the curve fitting procedure.

Atom probe tomography (APT) analysis was conducted on the as-anodized a-AM20 and corroded a-AM20 after potentiodynamic polarization tests for 1.5 h in 0.6 M NaCl aqueous solution. The sample surface was protected by depositing a $60-100$ nm Ni layer using a South Bay Technologies ion beam deposition system. APT specimens were made using a Thermo Fisher Nova 200 dual beam focused ion beam (FIB)/scanning electron microscope (SEM) with standard lift out and needle fabrication methods described by Thompson et al. [28]. An equilateral triangular prism was cut and lifted out, mounted on Si microtip array posts, and sharpened using a 30 kV Ga^+ ion beam. Pt from the needle surface was removed using a 2 kV ion beam until the deposited Ni above the oxide layer was at the needle surface. The APT experiment was run on a CAMECA LEAP 4000XHR using laser mode with a 30 K base temperature, 40–50 pJ laser power, a $0.2-0.5$ % detection rate, and a 200 kHz pulse repetition rate. The APT results were reconstructed and analyzed using CAMECA's interactive visualization and analysis software (IVAS 3.8).

3. Simulation procedure

In this work, the slab models were used to investigate the oxidation process on amorphous, nanocrystalline and single crystalline Al surfaces. Due to the absence of a reliable interatomic potential of the Al-Mn-O system, the simulation results reported here mainly focused on the oxidation of pure Al, while results on that of Al-Mn were provided in the supplementary material by using mixed interatomic potentials for Al-Mn, Al-O, and Mn-O, respectively (Fig. S1). The single crystalline Al slab was built by cleaving the (001) or (111) plane of Al crystal with a total of ~50, 000 atoms. For the nanocrystalline Al slab, a columnar structure with (111) texture parallel to the oxidation direction (i.e., z direction in Fig. 9) and an average grain size of 2.5 nm was constructed. Its surface area was similar to that of the single crystal. The amorphous Al slab was obtained by heating the Al single crystal with ~ 50,000 atoms from 0 to 2000 K, and then quenched to 300 K at a rate of 0.02 K/fs. For simulations at high temperatures (up to 800 K), each Al slab was relaxed by using isothermal isobaric (NPT) ensemble under zero pressure at the corresponding temperature. All relaxed Al slabs had similar sizes, i.e., $101.25 \times 101.25 \times 81$ Å along the x, y, and z directions of the simulation cell. Each Al slab was then placed in the simulation cell ($101.25 \times 101.25 \times 181$ Å) with 4000 O atoms by following a similar procedure to that reported by Campbell et al. [29], as shown in Fig. 9. Periodic boundary conditions were applied along all directions along the simulation cell.

After construction, each model was simulated at 300 K–800 K for 20 ps under canonical (NVT) ensemble, during which the oxidation occurred. All simulations were performed using the LAMMPS program [30] with the interatomic interactions between Al and O being modeled by the Reactive Force Field (ReaxFF) [31]. The time step was 0.4 fs and the Nose [32]/Hoover [33] thermostat was used to control the temperature. It was noticed that the oxidation process completed within 20 ps relaxation process and the thickness of the oxide layer remained unchanged after 20 ps. The atomistic structure of the formed oxide film in each model was analyzed by Ovito [34].

Table 1
Summary of parameters in sputter depth profile.

Element	Number of sweeps	Step size (eV)	Passage energy (eV)
Al 2p	10	0.125	69
Mn 2p	10	0.125	140
O 1s	8	0.05	26

4. Experimental results

4.1. XRD characterization

Fig. 2 shows the XRD results of all samples. Pure Al and Al 3003 exhibit a single face-centered-cubic phase with a strong (200) texture parallel to the sample normal direction. A broad peak was observed around $42-43°$ for AM20, indicating the formation of largely amorphous microstructure, in consistent with prior works on electrodeposited or sputtered Al-Mn alloys with similar compositions [10,16,18,20]. Compared to AM20, the structure of a-AM20 does not change after anodizing. A small feature at ~ 34.8° was also observed in both AM20 and a-AM20, close to the (104) diffraction peak of corundum (α-Al_2O_3) (JCPDS-ICDD File No 46-1212).

4.2. Corrosion behavior

Representative PD curves and the PD results of all samples are shown in Fig. 3. The passive regions of AM20 and a-AM20 are much wider than those of Al3003 and pure Al. The pitting potential increased with increasing Mn content in Al, as shown in Fig. 3(b). In addition, the protectiveness of naturally formed passive layer on AM20 can be further improved by anodizing the alloy surface, similar to those reported on other Al-based alloys [35,36]. Fig. 4(a) shows the Nyquist plots of all samples obtained after immersion in 0.6 M NaCl aqueous solution at room temperature for 300 s under E_{ocp}. The diameter of the capacitive semicircle is largest for a-AM20, followed by AM20, Al3003 and pure Al, indicating the enhanced protectiveness of the passive layer after alloying and anodizing, consistent with the PD results. The Bode plots of all samples are shown in Fig. 4(c) and (d). At high frequencies, the electrolyte resistance R_s was estimated to be ~ 11–15 Ω from Fig. 4(c). At lower frequencies, the polarization resistance increases in the sequence of pure Al, Al 3003, AM20, and a-AM20, in agreement with their PD behavior. The phase shift Bode plot (Fig. 4(d)) shows a wave trough for all samples in the low frequency region, characteristic of an

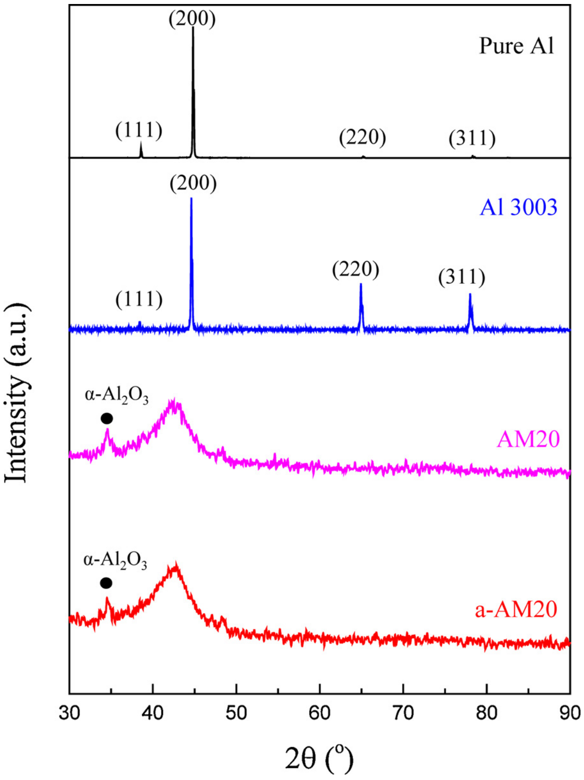

Fig. 2. The X-ray diffraction patterns of pure Al, Al3003, as-deposited Al-20at.%Mn (AM20), and anodized Al-20at.%Mn (a-AM20).

electrical circuit with two relaxation processes. Sample a-AM20 exhibited a maximum phase angle close to – 90° over a wide frequency range of 0.1 Hz–100 Hz (Figs. 4(d)), indicating its good capacitive response, while all others showed narrower frequency range of the capacitive effect.

The Nyquist and Bode plots were fitted using an equivalent circuit model shown in Fig. 4**(b)**, where R_s represents the ohmic solution resistance, R_1 is the charge transfer resistance, R_2 is the electrolytic resistance through the passive layer defects, the constant phase element CPE_1 and CPE_2 represent the non-ideal capacitive behavior of the double layer and the passive layer respectively. The double layer is formed between the metal surface and the electrolyte. As ions from the electrolyte is adsorbed onto the metal surface, the charged metal surface is separated from the charged ions in the electrolyte by an insulating surface (typically on the orders of angstroms) to form a capacitor CPE_1. The geometrical capacitance of the passive layer, which is mainly a metal oxide layer, as shown later in Section 4.3, corresponds to CPE_2. This model represents just one of several possible equivalent circuits that can fit the measured EIS data. It is chosen due to its inclusion of two relaxation processes, and the fact that it has been successfully adopted in prior research for Al-Mn [11,21] and Al-W [37] solid solutions in NaCl electrolytes. Table 2 summarizes the model fitting parameters. The impedance of the CPE is defined as $Z = \frac{1}{Y_0(j\omega)^n}$, Y_0 is a constant, j is the imaginary unit, ω is the angular frequency of the sinusoidal signal, and n is an exponent in the range of $0 < n < 1$. When n = 1, the CPE behaves like an ideal capacitor; when n = 0, it behaves like a pure resistor. For CPE_2, the n_2 value increases from 0.813 for pure Al to 0.949 for a-AM20, indicating a more ideal capacitor behavior in the later. The thickness of the passive layer d was estimated by [38]

$$d = \varepsilon\varepsilon_0 A/C \quad (1)$$

where ε_0 is the vacuum dielectric constant ($\varepsilon_0 = 8.85 \times 10^{-14} F{\bullet}cm^{-1}$), ε is the dielectric constant (relative electric permittivity) of barrier-type alumina (ε= 20), A is the area exposed to the electrolyte solution (~ 1 cm^2), and C is the capacitance from CPE_2. Table 2 shows that the values of CPE_2 increases in the order of pure Al, Al3003, a-AM20, and AM20. Hence the calculated passive layer thickness decreases in that same order. The passive layer thickness on a-AM20 is ~ 4.62 nm, which is slightly higher than that on AM20 (~ 4.09 nm) but smaller than that on Al3003 (6.94 nm) and pure Al (7.25 nm).

4.3. Surface characterization via XPS

Fig. 5 shows the element depth profile measured from XPS over 24 sputtering cycles, where the metal/oxide interface was defined by a change of bulk alloy concentration by ~ 10 %. It can be seen that the trend of surface oxide layer thickness of all samples is consistent with the EIS results. Mn was absent from Al3003 due to its low concentrations (~ 0.6 at.%). In AM20 and a-AM20, Mn concentration decreases from 20 at.% at the metal/oxide interface to zero at the oxide surface, confirming their selective dissolution in the passive layer. In the outer surface of the oxide, the composition of oxide is ~ $Al_{33}O_{67}$ for pure Al, $Al_{36}O_{64}$ for Al3003, and $Al_{40}O_{60}$ for AM20 and a-AM20. Such results indicate that ~ 20 at.% Mn addition in these alloys and its selective surface dissolution brings the surface oxide composition to the exact stoichiometry of its stable oxide (i.e. corundum Al_2O_3).

Fig. 6 summarizes the Al 2p, O 1s and Mn 2p core levels for all samples as a function of sputtering cycle, where cycle 1 corresponds to the outmost surface. Additional figures of the Al 2p spectra fitting of selected samples are provided in the supplementary materials (Fig. S2-S3). For pure Al, the outer surface contains aluminum oxide, AlO(OH) and a small amount of Al-Al bond. The intensities of both aluminum oxide and AlO(OH) dramatically decreases after 24 cycles (~ 10 min sputtering time), while the O content around 25 at.% can still be

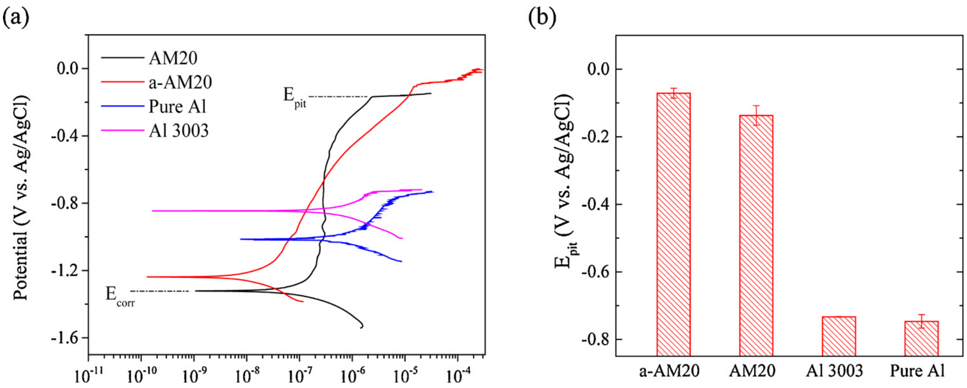

Fig. 3. (a) Representative potentiodynamic polarization curves and (b) summary of pitting potential of all samples after corrosion in 0.6 M NaCl solution at room temperature.

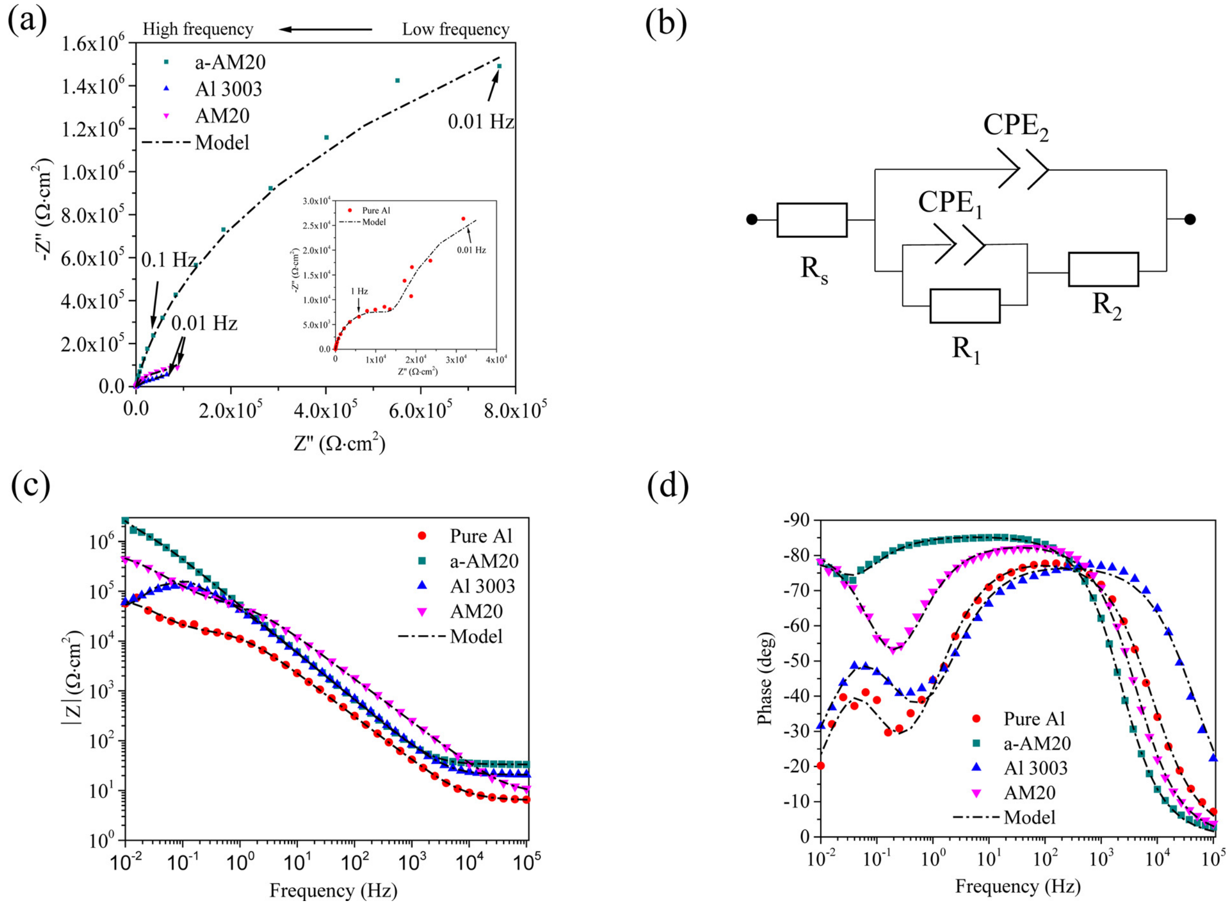

Fig. 4. (a) Nyquist plot of EIS measurements and model fit and (b) the equivalent circuit model used for the model fitting in (a). Bode plot of the impedance (c) magnitude and (d) phase shift angle as a function of frequency from EIS measurements of all samples at open circuit potential in 0.6 M NaCl solution.

Table 2
Summary of equivalent circuit model fitting parameters defined in Fig. 4(b).

Sample	R_s (Ω)	R_1 (Ω)	Y_1 ($cm^2S^{-n}\Omega$)	n_1	CPE_1(F)	R_2 (Ω)	Y_2 ($cm^2S^{-n}\Omega$)	n_2	CPE_2(F)	d (nm)
Pure Al	10.95	2.00×10^4	1.93×10^{-5}	0.838	1.61×10^{-5}	3.69×10^4	3.84×10^{-6}	0.813	2.45×10^{-6}	7.25
Al 3003	14.88	$5.02 x10^4$	2.70×10^{-5}	0.869	2.83×10^{-5}	5.93×10^4	3.54×10^{-6}	0.826	2.55×10^{-6}	6.94
AM20	14.59	$8.43 x10^4$	5.23×10^{-5}	0.947	5.69×10^{-5}	4.28×10^5	$4.13 x10^{-6}$	0.922	4.33×10^{-6}	4.09
a-AM20	13.90	9.30×10^4	5.75×10^{-5}	0.967	6.09×10^{-5}	2.63×10^6	3.41×10^{-6}	0.949	3.83×10^{-6}	4.62

detected. A similar trend was also observed for Al 3003. Aluminum oxide, AlO(OH) and $Al(OH)_3$ have been detected near the top surface of a-AM20 before and after potentiodynamic polarization for 1.5 h while only Al oxide and AlO(OH) have been detected for AM20. In terms of Mn 2p spectra, for both AM20 and a-AM20, Mn remains in the elemental form throughout the surface oxide layer, with extremely low concentrations in the first three cycles (~ 2 min sputtering time), while those of Mn oxide species was absent (whose binding energy is at 640.5 eV and 642.3 eV). A similar behavior was observed for corroded a-AM20, with the exception that a very small intensity of MnO_2 was detected on the outmost surface (cycle 1). This observation is somewhat in agreement with prior research. For example, Zhang et al. [21] showed that Mn is present on the surface of anodized Al-Mn but becomes absent after long term (2808 h) immersion in NaCl aqueous solution.

4.4. APT results

To further understand the atomic structure of the oxide layer that provided the corrosion protection on the metal surface, APT analysis was performed on selected samples with the results presented in Fig. 7. APT atom maps are shown in Fig. 7(a) and (b) for the a-AM20 sample before and after corrosion. Fig. 7(c) and (d) display the 1D concentration profiles of the oxide/alloy interfaces, which were calculated using proximity histograms of 10 at.% O isoconcentration surfaces within density corrected (using the Z-redistribution algorithm) 15 × 15 × 50 nm ROIs extracted from the center of the dataset [39,40]. The results show ~ 4 nm and 8 nm surface oxide layers formed on a-AM20 before and after PD corrosion, respectively. The thickness of a-AM20 before corrosion is in good agreement with the EIS results (4.78 nm). In both cases, the oxide layer is mainly enriched in Al and O with an Al/O ratio close to 2:1, while that of Mn is largely absent, as shown in Fig. 7(c) and (d). The MnO mass spectral peaks were found to be basically zero in the oxide layer and the metal substrate. Such results are consistent with our prior TEM analysis on anodized $Al_{80}Mn_{20}$ after tribocorrosion [41]. Interestingly, in both cases, a slight enrichment of Mn near the oxide/metal interface was also observed, similar to those reported previously in anodized Al-Mn alloys [23].

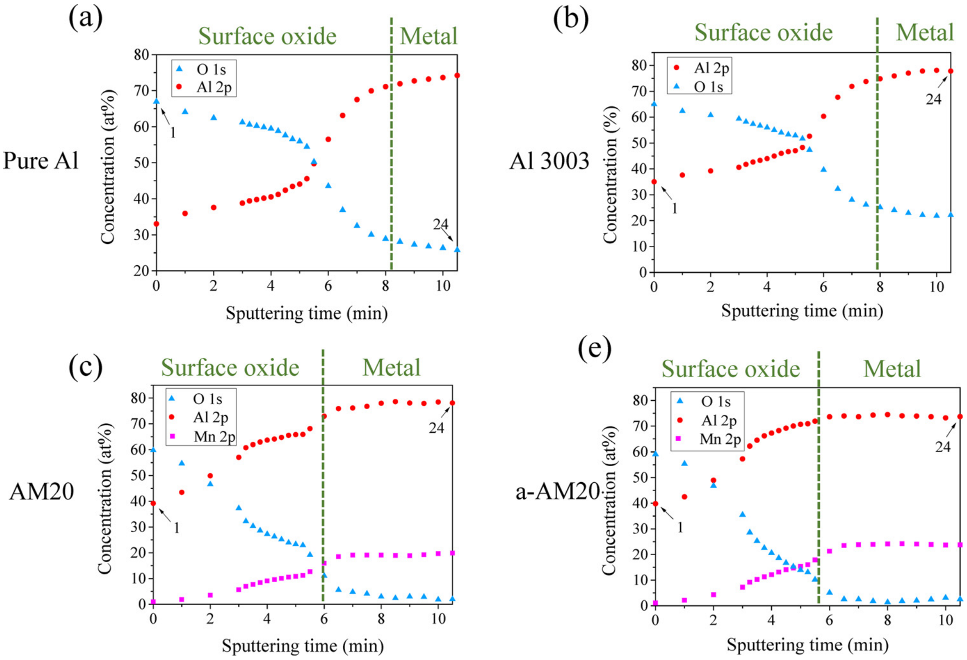

Fig. 5. XPS depth-profile for O, Al, and Mn elements of all samples.

4.5. Defect characterization by Mott-Schottky (M–S) analysis

Fig. 8 summarizes the M–S analysis results of all samples. Here, the capacitance of the Helmholtz layer is assumed to be much bigger than the semiconductor capacitance of the passive layer, hence the measured capacitance of the interfacial double layer C is taken as the semiconductor capacitance of the passive layer to calculate the defect densities according to the following equation [42–46]

$$\frac{1}{C^2} = \frac{\pm 2}{\varepsilon\varepsilon_0 eN}\left(E - E_{fb} - \frac{kT}{e}\right) \tag{2}$$

where C is the capacitance, ε is the passive film dielectric constant (10 for Al_2O_3 [47]), ε_o is the permittivity of vacuum ($\varepsilon_o = 8.85 \times 10^{-14}$ F/cm), N is the dopant density, E is the applied potential, E_{fb} is the flat band potential, k is the Boltzmann constant (1.38×10^{-23} JK^{-1}), T is the absolute temperature, and e is the elementary charge (1.602×10^{-19} C). It was found that while only n-type defects such as oxygen vacancies and cation interstitials (e.g. Al^{3+}) were observed in pure Al, all Al-Mn alloys contain p-type defect (e.g. cation vacancies) at low potentials and n-type defect at high potentials. As Mn% increases, the density of n-type defect decreases while that of p-type increases (except after anodizing). These results indicate alloying with Mn changed the metal-excess oxide (n-type) of Al into a metal-deficit (p-type) oxide at low potentials, most likely due to the selective dissolution of Mn, thus leaving behind cation vacancies. At higher potentials, with increased population of Al^{3+} interstitials due to polarization, the surface oxide becomes n-type again, but with lower defect density than pure Al, probably due to the originally lower (or absent) O^{2-} vacancies and Al^{3+} interstitials. A similar "V-shaped" p-n junction behavior has also been reported for anodic aluminum oxide films [48], passive films formed on Fe-based amorphous alloys after corrosion in acetic acid [49], and those on AISI 304 stainless steel in NaCl aqueous solution [50]. In the present work, such p-n junction could be interpreted as two capacitors in series, one corresponding to the p-Al_2O_3/n-Al_2O_3 interface and the other to the n-Al_2O_3/electrolyte interface [51].

Fig. 8(c) summarizes the n-type defect density and pitting potential of all samples. It can be seen that as the n-type defect density decreases, the pitting potential increases. This is in good agreement with the classical point defect theory [52], which assumes that pitting corrosion initiates at the oxide/solution interface involving the adsorption of chloride ions into oxygen vacancies [52]. Hence a reduced n-type defect density leads to reduced chloride adsorption, and better pitting resistance. Although not fully understood at this point, these results indicate the complex defect state due to selective dissolution of the solute element Mn at different potentials.

5. MD simulation results

5.1. Oxidation of crystalline vs. amorphous Al surface

The above APT and XPS results have shown that in the surface oxide layer of AM20 and a-AM20, only aluminum (hydr)oxide was present while Mn was present in the non-oxidized metal form (Mn°), with a decreasing concentration from 20 at.% Mn (bulk concentration) at the metal/oxide interface to zero at the outermost (hydr)oxide surface. In other words, Mn addition enhanced the corrosion resistance of Al without participating in the surface oxidation. To gain a better understanding of the passive layer formation (i.e. oxidation) mechanisms of Al and Al-Mn, MD simulations were performed. Ideally, such simulations would be performed on crystalline Al, amorphous Al, and amorphous Al-Mn to take into accounts of both structural and compositional differences. However, due to the lack of a reliable interatomic potential of the Al-Mn-O system, the present work mainly focuses on the pure Al system, while results on the oxidation of amorphous Al-Mn are provided in the supplementary material. Since crystalline Al, amorphous Al, and amorphous Al-Mn represents a trend of increased Al-Al bond distance and free volume, it is assumed that the trend from crystalline to amorphous Al could be potentially extended to Al-Mn, where the presence of Mn further increased the Al-Al bond distance and free volume but does not participate in the oxidation process.

Fig. 9 shows that during the oxidation process of amorphous and single crystalline Al (001), the O atoms moved inwards while the Al atoms moved outwards to form the oxide films. Both films had similar thickness of about two atomic layers, as shown in Fig.9(c), (f). A closer comparison of the atomic structure of the oxide films indicates that there were fewer holes in the oxide film on the amorphous Al than that on the single crystalline Al surface (Fig. 10(a),(b)). Since the formed oxide films on both surfaces had similar thickness and area, the density

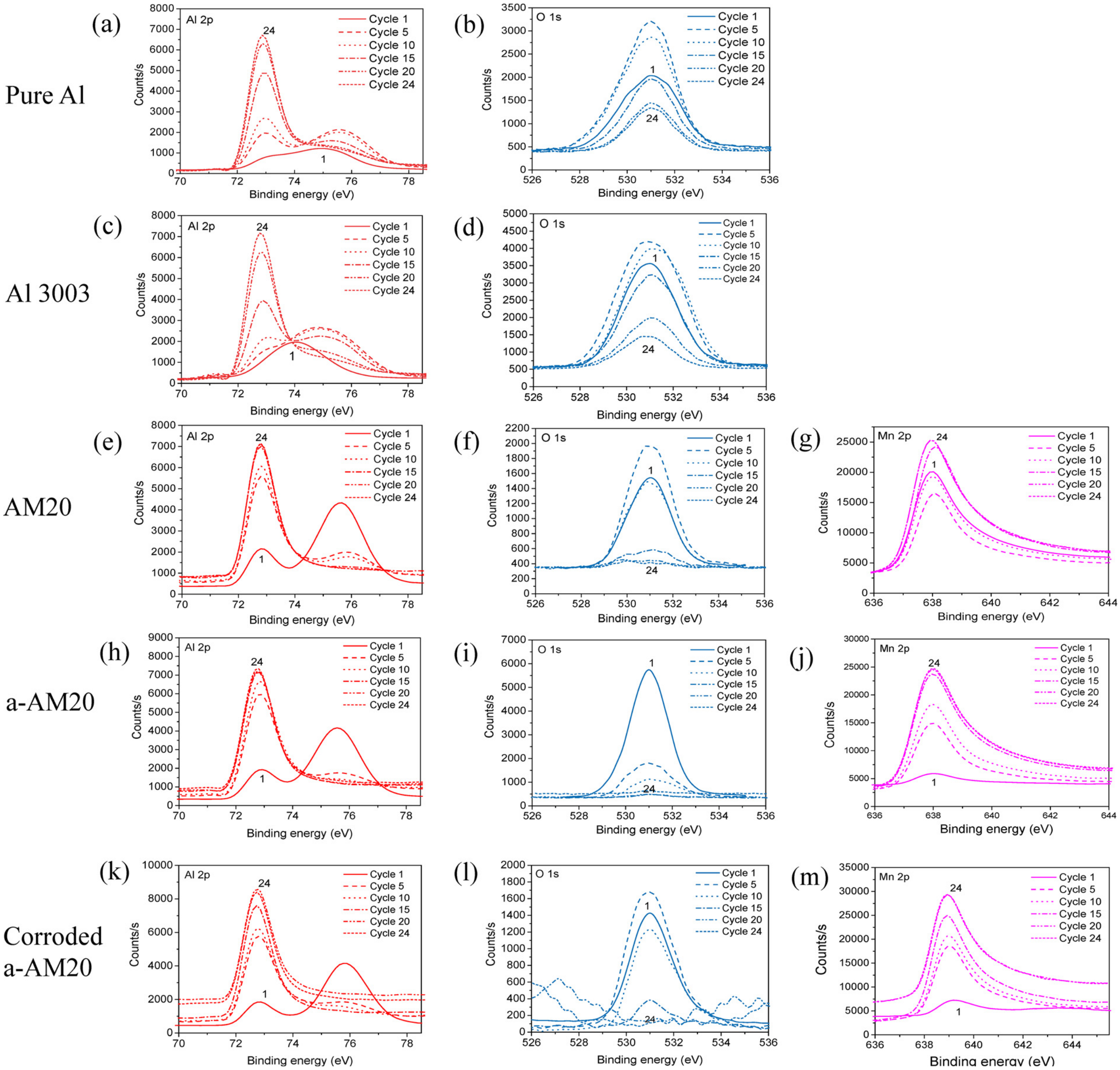

Fig. 6. XPS depth-profile of Al 2p, O 1s, and Mn 2p spectra for all samples.

of these two oxide films can be quantified by using the number of Al-O bonds present. As shown in Fig. 10(c), the number of Al-O bonds of amorphous Al was higher than that of single crystalline Al, consistent with the visual inspection based on the atomic structures. Results based on additional simulations at 800 K (Fig. 10 (d)-(f)) showed a similar trend.

5.2. The oxidation activation energy

To quantify the thermodynamic driving forces for the oxidation process, the oxidation activation energy was investigated for both crystalline and amorphous Al, as shown in Fig. 11. Based on the number of Al-O bond formed at different temperatures (Fig.11(a), (b)), the average oxidation velocity was calculated by linearly fitting the time-dependent Al-O bond number between 0.4 and 2.4 ps. An example of such fitting process was included in Fig. 11(c). The extracted oxidation velocity was then plotted against temperature and fitted in Fig. 11(d) by assuming an Arrhenius relation, i.e., $V = V_0\exp(-E/kT)$, where V is oxidation velocity, V_0 is pre-exponential factor, E is activation energy, k is the Boltzmann constant and T is the temperature. The fitted activation energy E was found to be 0.0086 eV and 0.0107 eV for amorphous and single crystalline Al respectively, indicating that the oxidation on the amorphous Al was more energetically favorable than that on the single crystalline Al.

5.3. Atomic pathway of oxidation process

The atomic pathway of Al and O atoms during the oxidation process was found to be dramatically different on the amorphous and single crystalline Al surfaces. The findings at 300 K were presented in Fig. 12 as an example. On the amorphous Al surface (Fig. 12(a) and (b)), Al atoms were first pulled out of the topmost surface layer, creating vacancies in their original position. Almost simultaneously, the nearby oxygen atoms would fall into the vacancies and become bonded with the surrounding Al atoms. This mechanism was consistent with that reported by Campbell et al. [29]. In contrast, during oxidation on the single crystalline Al surface (Fig. 12(c)-(e)), O atoms moved into the tetrahedral and octahedral sites in the Al lattice, during which at least four surrounding Al atoms became deviated from their original lattice sites and were pulled out of the free surface (Fig. 12(d)). Therefore, when the O atoms moved towards these sites, more energy was needed as compared to that on the amorphous Al surface. In addition, the

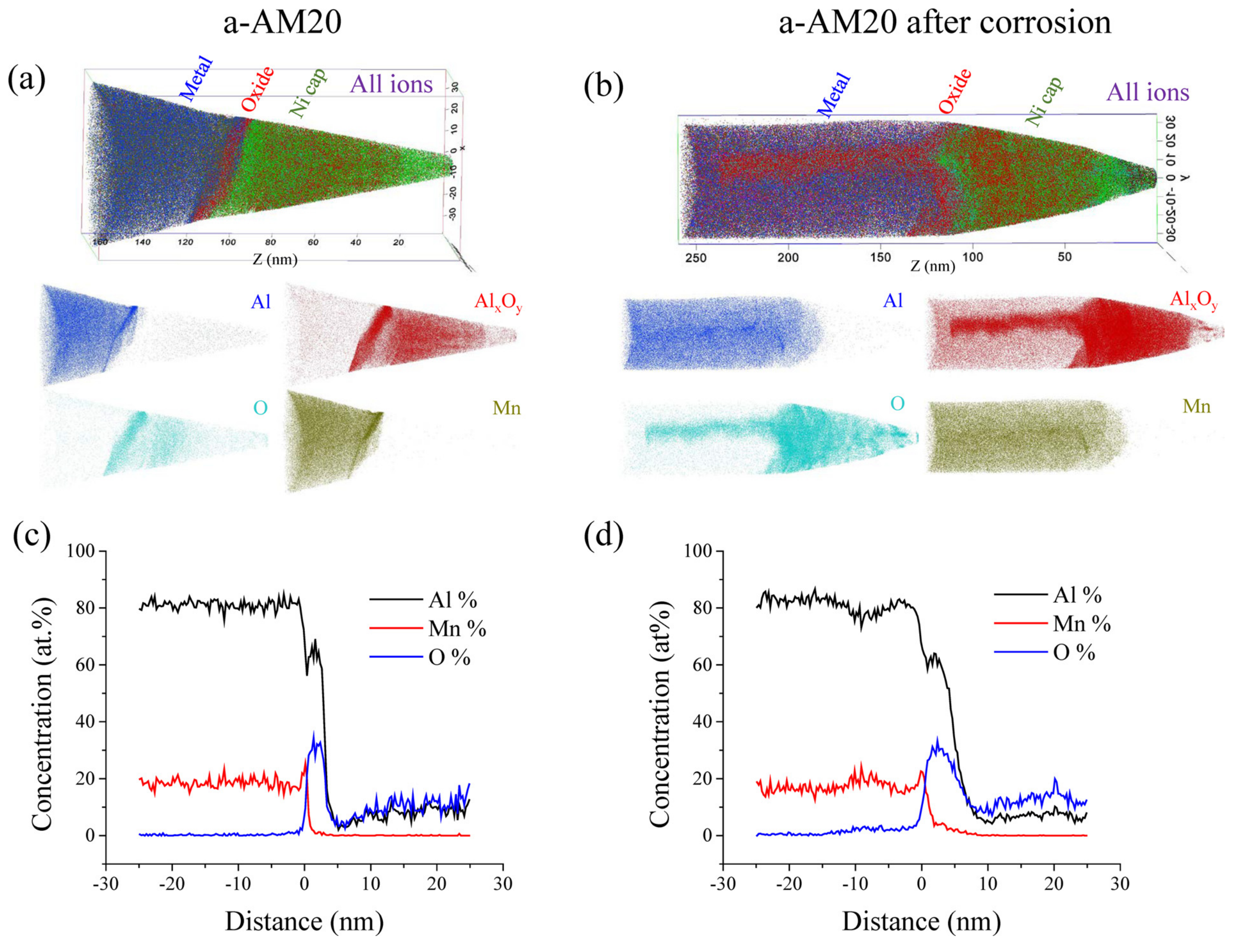

Fig. 7. 3D re-constructed surface of (b) a-AM20 and (b) a-AM20 after corrosion, and (b, d) element concentration line profile of the 3D re-constructed surfaces.

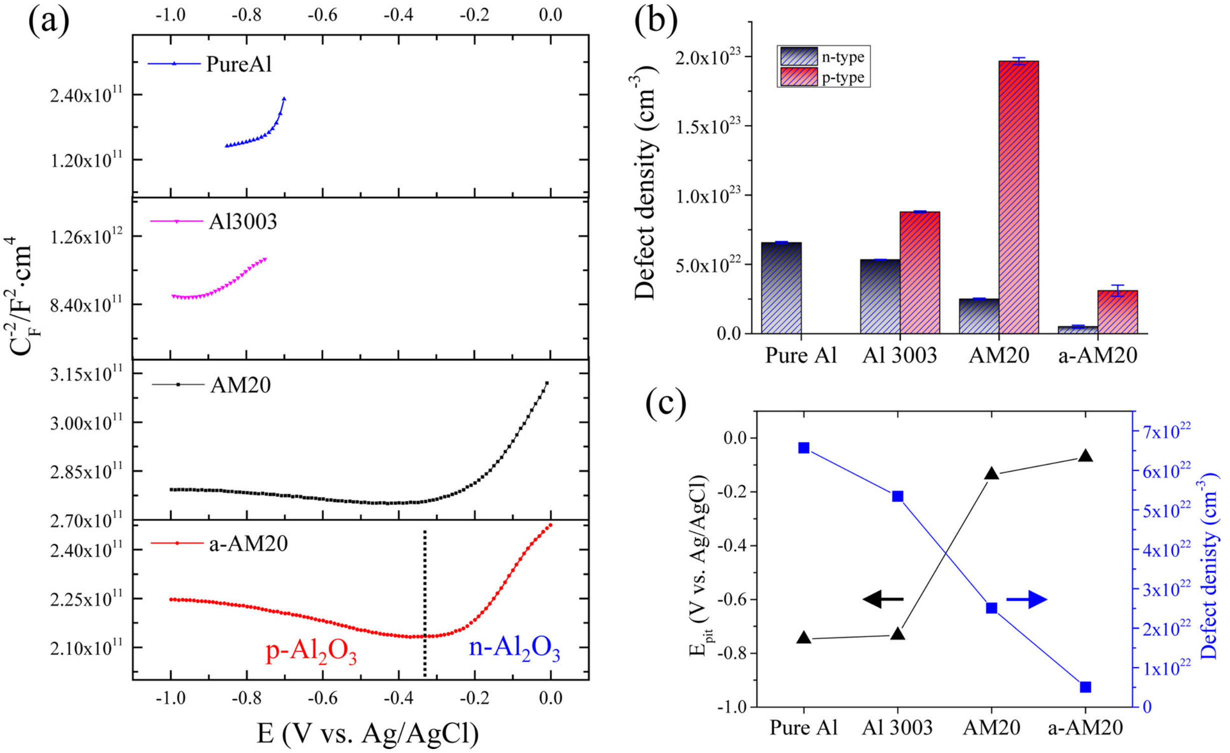

Fig. 8. (a) Summary of Mott–Schottky plots, (b) defect density, and (c) n-type defects v.s. pitting potential E_{pit} of all samples.

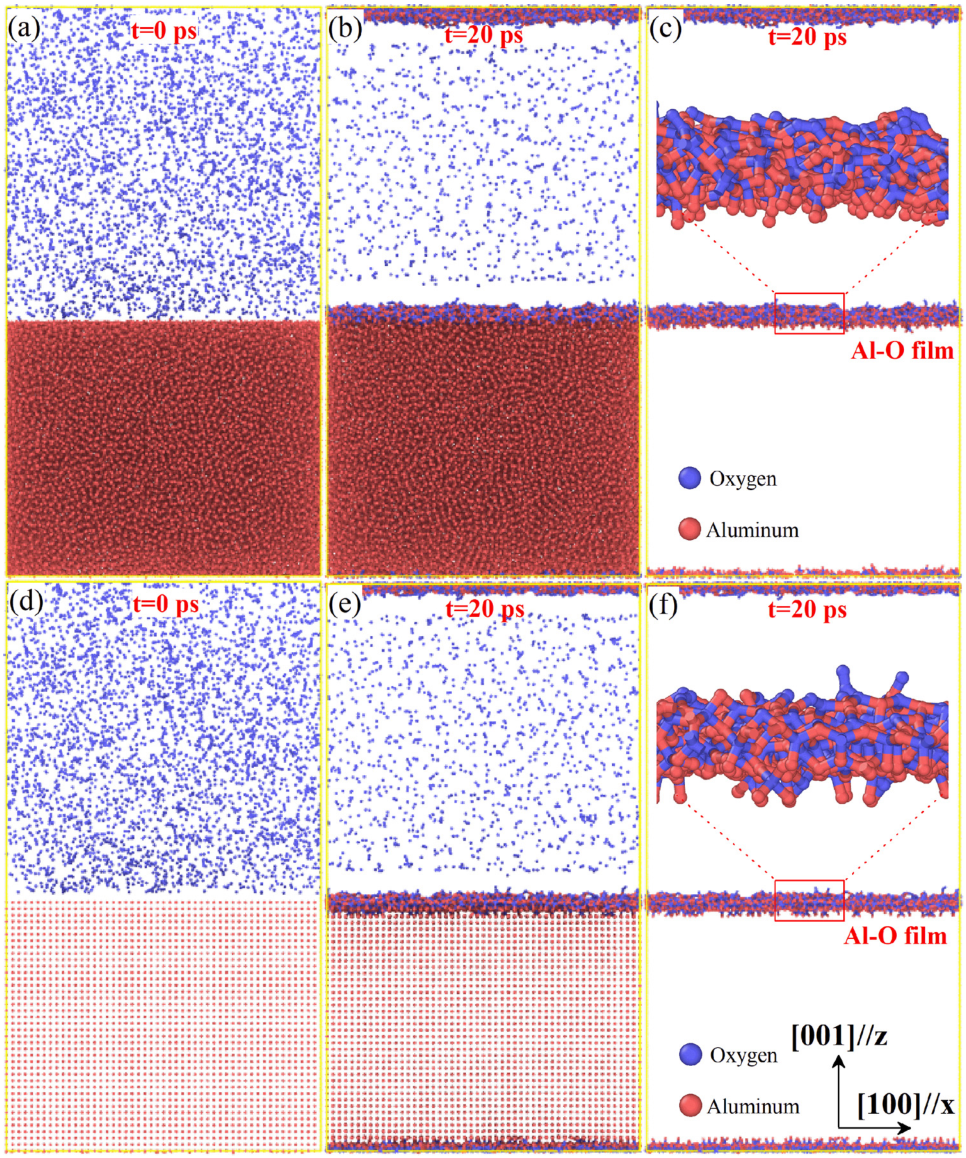

Fig. 9. The (a, d) initial and (b.e) final plane view and (c, f) cross-sectional view of the amorphous and single crystalline Al (001) slab after 20 ps of oxidation.

number of tetrahedral and octahedral sites was limited (eight tetrahedral sites and four octahedral sites per unit cell) in the single crystalline Al while on the amorphous Al surface, every Al atom could be potentially pulled out and become a vacancy. Due to these reasons, the amorphous Al surface can absorb more O atoms with lower activation energy, thus forming much denser oxide film than that on the single crystalline Al surface.

The different oxidation mechanisms on the amorphous and single crystalline Al surfaces suggest that increasing the free volume in Al promotes the formation of denser oxide film. To further confirm this result, the oxidation on nanograined (~ 2.5 nm grain size) and single crystalline Al (111) plane were also simulated. The atomic configuration of the oxide film and the number of Al-O bonds on each Al surface are presented in Fig. 13. The oxide film on the nanograined Al surface appeared to be denser (with less holes) than that on the single crystalline Al surface, but less so than that on the amorphous Al surface. This trend is consistent with the number of Al-O bond for each oxide film (Fig. 13(c)). It is worth noting that the number of Al-O bonds in the oxide film on the single crystalline Al (001) plane was similar to single crystalline Al (111) plane (Fig. 13(f)). Therefore, the crystal orientation has little impact on the density of oxide film, and a more practical strategy to improve the density of oxide film on the Al surface is to increase the free volume or Al-Al bond distance via alloying with a non-passive element such as Mn.

6. Discussion

Corrosion resistance of complex alloys depends heavily on the structure and property of the surface oxide layer. Generally speaking, both the composition and crystal structure of the oxide layer are far from equilibrium in the surface oxide layer of complex alloys. Such complexity makes theory-guided alloy design and selection rather challenging. In the present work, we show that when alloyed with non-passive element Mn in solid solution, the corrosion resistance of Al was significantly enhanced although Mn is largely absent from the passive layer. Such results cannot be explained by only considering the thermodynamics during corrosion. For example, the calculated potential/pH (Pourbaix) diagram of $Al_{80}Mn_{20}$ is shown in Fig. 14 following algorithms in [53,54]. It can be seen that near neutral pH, the passivity region of $Al_{80}Mn_{20}$ is very similar to pure Al. In other words, the addition of Mn does not increase the passivity region of the alloy because Mn is dissolving/corroding under such pH/potential condition. Due to

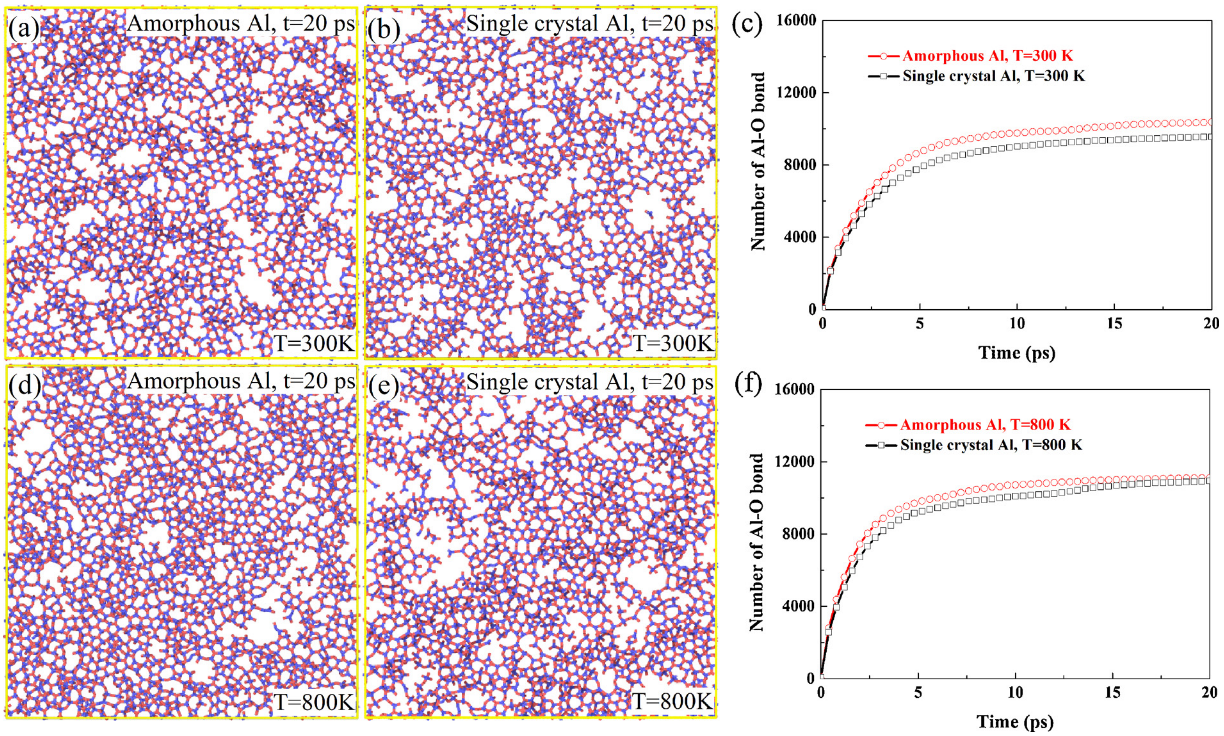

Fig. 10. Structure of the oxide film on the amorphous and single crystalline Al surface at (a-b) 300 K and (d-e) 800 K, and the number of Al-O bonds in the oxide film formed on the amorphous and single crystalline Al surface at (c) 300 K and (f) 800 K.

this reason, the effect of Mn must be related to the corrosion kinetics.

Specifically, our experimental study shows that increasing Mn% in Al enhanced its pitting resistance and reduced its corrosion rate compared to pure Al. This corrosion protection was further enhanced by anodizing, where the passive film thickness slightly increased, with reduced p-type defect density. Through comprehensive surface characterization, we found that the selective dissolution of Mn facilitate the formation of a thinner oxide layer with closer to stoichiometric composition than that on pure Al. At the same time, the surface depletion of Mn reduces the n-type defect density in the passivation layer that further affects charge transfer and chloride adsorption. MD simulations on crystalline and amorphous Al further confirm that increasing the free volume content and Al-Al bond distance lead to lower activation energy and more O transport pathways of amorphous Al, and hence the formation of a denser oxide layer.

Several observations are interesting: (1) the oxide layer on Al-Mn alloys are thicker than that on pure Al, and the oxide thickness decreases with increasing Mn content (by comparing those on Al 3003 and AM20); (2) the defect type is n-type in pure Al, but p-n junction for all Al-Mn alloys studied. In addition, the total defect density in the alloy is

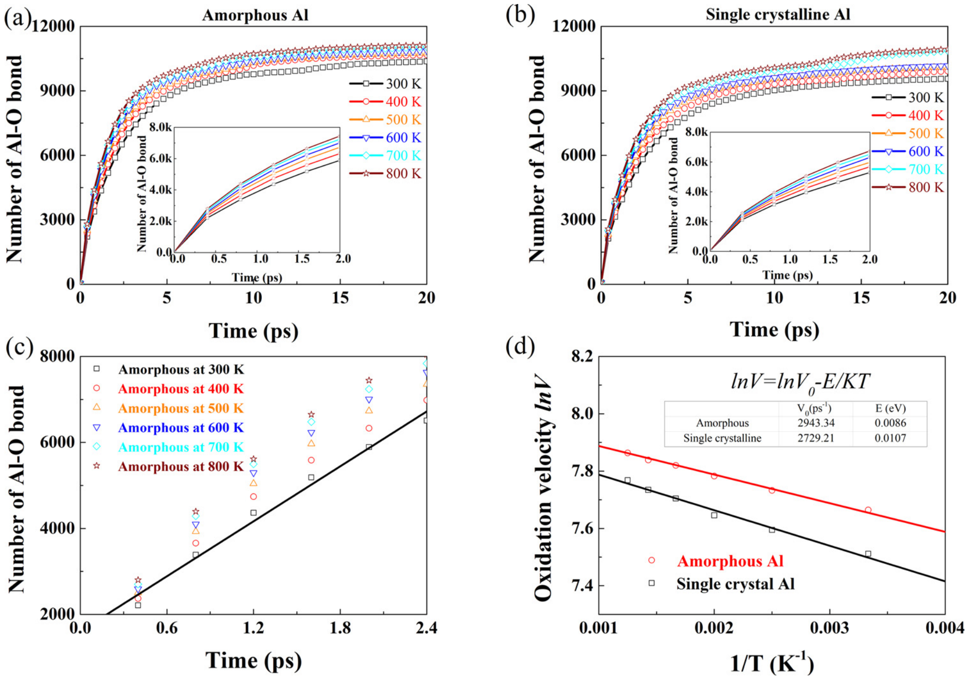

Fig. 11. The number of Al-O bonds in the oxide film formed on the (a) amorphous and (b) single crystalline Al surface at different temperatures. (c) The number of Al-O bonds on the amorphous Al surface during the initial stage (0.4 - 2.4 ps) and (d) oxidation velocity on the amorphous and single crystalline Al surface at different temperatures, where the solid lines were fitted based on the Arrhenius equation $V = V_0\exp(-E/kT)$. The fitted velocity constant V_0 and activation energy E for oxidation were included in the inset of (d).

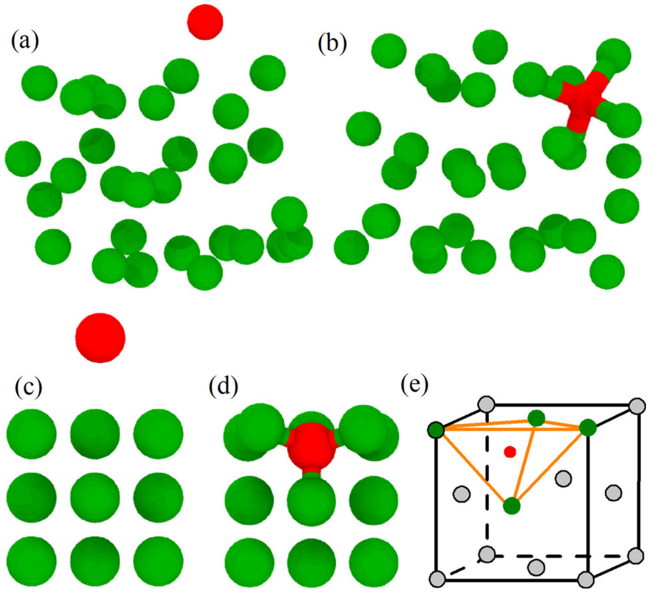

Fig. 12. Atomic pathway of oxidation process on the amorphous and single crystalline Al surface. (a), (b) Oxidation process on the amorphous Al surface. (c), (d) Oxidation process on the single crystalline Al surface. (e) The schematic of Al unit cell highlighting the tetrahedral site occupied by O. The red and green colors represent O and Al atoms, respectively (For interpretation of the references to colour in this figure legend, the reader is referred to the web version of this article).

higher at higher Mn%. Such results indicate that the effect of Mn is mostly in reducing mass transport, rather than electronic transport, by forming a more compact oxide layer. On one hand, MD simulations show that the amorphous Al forms an oxide layer with higher density. Such a high-density oxide layer would be effective in reducing oxygen transfer and diffusion, hence making further oxidation more difficult, thus producing a thinner oxide layer than pure Al, in agreement with the experimental observation. On the other hand, by comparing single crystal, nanocrystal, and amorphous Al, MD simulations clearly indicate that having a larger than equilibrium Al-Al bonding length facilitate the formation of a denser oxide, most likely due to the lattice mismatch between pure Al and Al_2O_3.

Finally, a simplistic model is proposed in Fig. 15 to explain the observed alloying effect by considering an effective Pilling-Bedworth (PB) ratio of a binary alloy and its implications on the structural compatibility between the metal and oxide. For a pure metal, PB ratio is defined as

$$R_{PB} = \frac{volume\ of\ oxide\ produced}{volume\ of\ metal\ consumed} = \frac{M_{oxide} \bullet \rho_{metal}}{nM_{metal} \bullet \rho_{oxide}}, \tag{1}$$

where M is the atomic or molecular mass, ρ is the density, and n is the number of metal atoms per molecule of the oxide [55]. Now consider a binary alloy of A_mB_n (where m% and n% are the atomic percentage of element A and B respectively). We define an effective PB ratio for the whole alloy as:

$$R_{PB}^{eff} = \sum_{i=1}^{n} x_i R_{PB}^{i} \tag{2}$$

where x_i is the atomic percentage of the passivating element i and R_{PB}^{i} is the corresponding PB ratio. Under a given corrosive environment, each constituting element's passivity can be identified thermodynamically from its Pourbaix diagram. Note here that this calculation does not include the PB ratio of any non-passivating elements in the alloy. We hypothesize that once the alloy composition is optimized to achieve an effective PB ratio close to 1, the naturally formed oxide layer is of the highest protectiveness by having high density and low porosity due to excellent structural compatibility between the oxide and the metal lattices (Fig. 15). Note that this parameter is formulated based on structural consideration, hence completely different from the empirical parameters such as pitting resistant equivalent number (PREN) used for steel design [56]. This compact surface oxide layer would be an

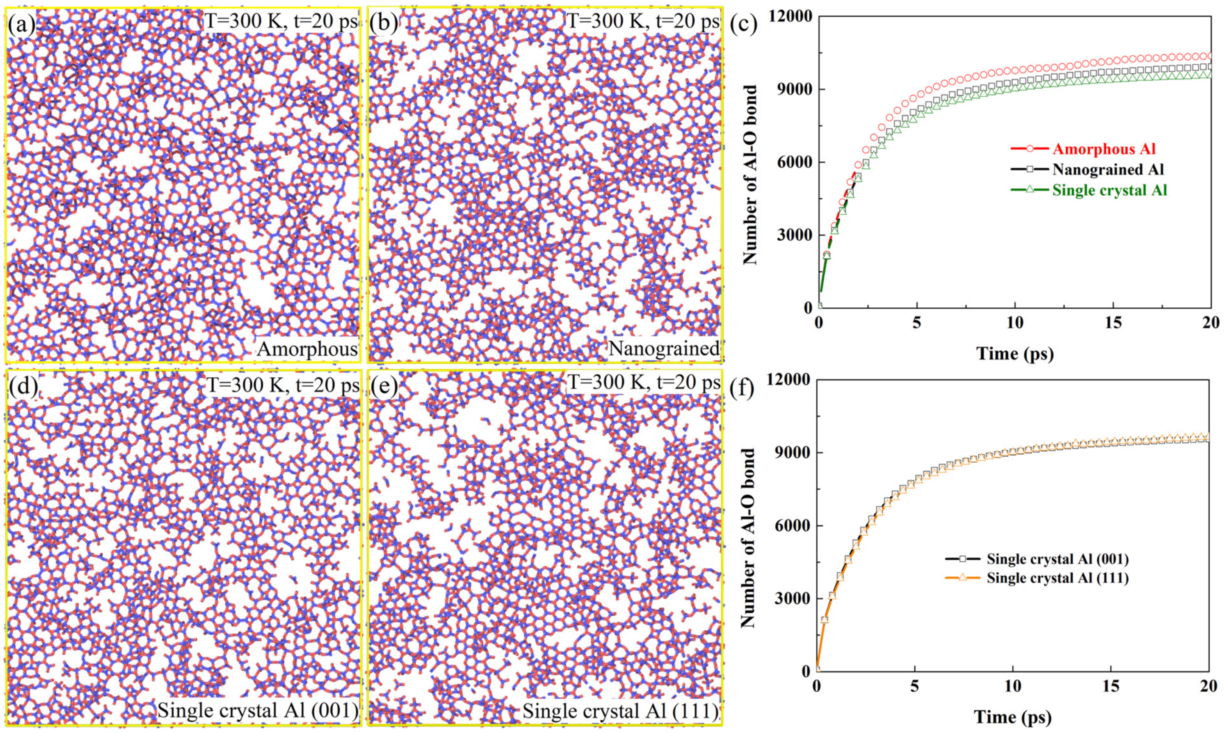

Fig. 13. Comparison of the oxide film structure among that formed on the (a) amorphous, (b) nanograined, (d) single crystalline (001) and (e) single crystalline (111) Al at 300 K. (c) The number of Al-O bonds in the oxide film formed on the amorphous, nanograined and single crystalline Al (001) surface. (f) The number of Al-O bonds in the oxide film formed on the single crystalline Al (001) and (111) surfaces.

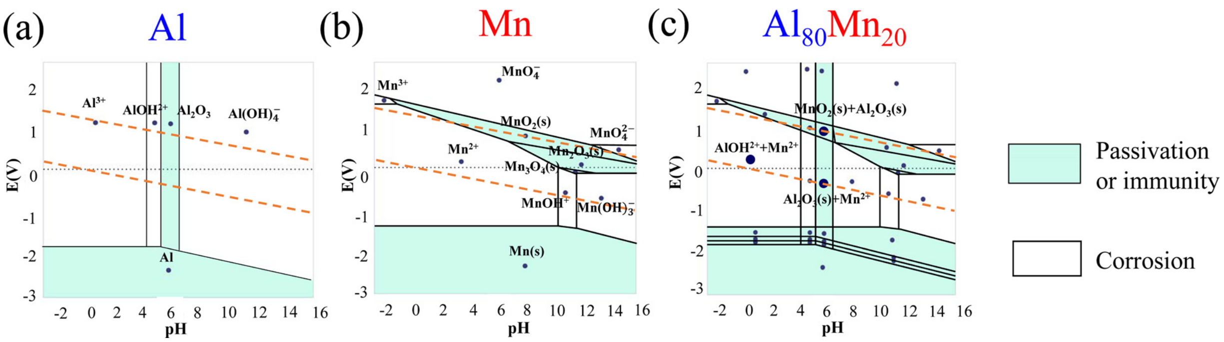

Fig. 14. Pourbaix diagrams of (a) Al, (b) Mn, and (c) $Al_{80}Mn_{20}$ alloys.

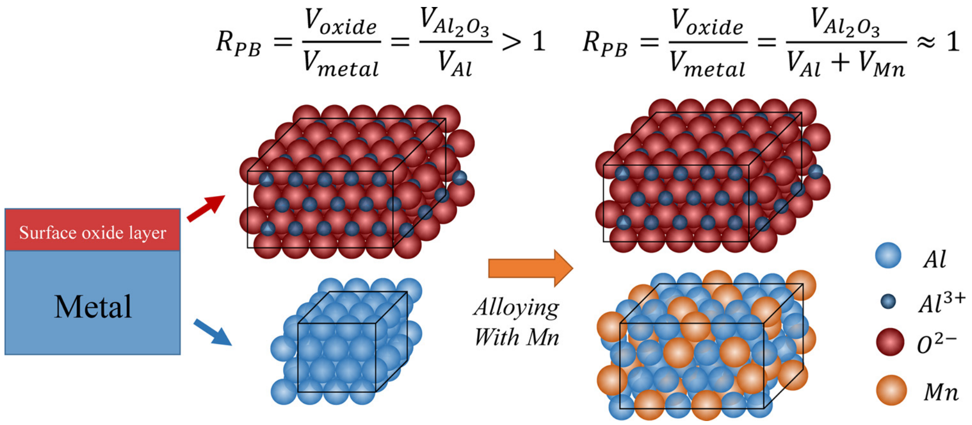

Fig. 15. Proposed selective solute dissolution model with schematics showing change of PB ratio of Al after alloying with Mn. We hypothesize that the oxide barrier characteristics can be tailored by alloying with non-passivating element (Mn) in solid solution, whose selective dissolution in the surface results in a PB ratio close to 1.

effective barrier to oxygen diffusion and, as a result, lead to the formation of a *thinner* oxide layer than those with a higher PB ratio. The three alloys studied here: pure Al, Al 3003 (1.6 at.% Mn), and AM20 (20 at.% Mn), having an R_{PB}^{eff} of 1.33, 1.31 and 1.06, respectively, indeed showed increased corrosion resistance and reduced oxide thickness, supporting our hypothesis. These PB ratios are calculated assuming the formation of α-Al_2O_3 (corundum, trigonal $R\bar{3}c$), as confirmed by XRD results in Fig. 2. Interestingly, this simple model can also explain why the pitting potential of Al-Mn starts to decrease when Mn% is above ~ 40 at.% [16], where its R_{PB}^{eff} becomes 0.8, significantly smaller than 1. Hence the formed oxide layer does not have enough volume to completely cover the metal substrate for effective passivation. Such a simplistic model needs future examination, especially from complex alloy systems such as high entropy alloys and metallic glasses. As a last note, the presence of a thin oxide layer, coupled with enhanced surface activity of Al, could also render a faster repassivation rate if the surface oxide layer is damaged, in agreement with our prior work [10].

7. Conclusions

A synergistic experimental and computational study was carried out to evaluate the effects of a non-passive element, Mn, on the aqueous corrosion behavior of a passive element, Al. It was found experimentally using APT and XPS that the corrosion resistance of Al increased with increasing Mn content (to 20 at.%) in the alloy, despite the fact that Mn does not participate in the surface oxidation process. Although the addition of Mn also changed the defect type and defect density in the oxide layer, its effect on corrosion kinetics is more related to the restriction of mass transport by forming a denser, thinner oxide layer with closer to stoichiometry composition due to the selective dissolution of Mn, resulting in a higher free volume than pure Al. MD simulations confirm that with an increasing free volume in Al, the density of the oxide layer increases due to the lower activation energy and more oxygen transport pathways. Finally, a simplistic model was proposed to guide future alloy design by considering the optimization of the passive and non-passive element ratio to achieve an optimum effective Pilling-Bedworth ratio of the system.

Data availability statement

The raw data required to reproduce these findings are available upon request from the corresponding authors.

CRediT authorship contribution statement

Jia Chen: Investigation, Validation, Writing - original draft. **Jianwei Xiao:** Methodology, Software, Writing - original draft. **Jonathan Poplawsky:** Investigation. **F. Marc Michel:** Investigation. **Chuang Deng:** Supervision, Writing - review & editing. **Wenjun Cai:** Conceptualization, Supervision, Writing - review & editing.

Declaration of Competing Interests

The authors declare that they have no known competing financial interests or personal relationships that could have appeared to influence the work reported in this paper.

Acknowledgements

This research was financially supported by the US National Science FoundationDMR-1856196. J.C. and W.C. gratefully acknowledge the discussion of XPS analysis and results with Dr. Weinan Leng of the Nanoscale Characterization and Fabrication Laboratory and Dr. David F. Cox of Chemical Engineering at Virginia Tech. Selected X-ray diffraction measurements were conducted at the Virginia Tech Crystallography (VTX) Lab with support from the Virginia Tech National Center for Earth and Environmental Nanotechnology Infrastructure (NanoEarth, NSF Cooperative Agreement 1542100). APT was conducted at the Center for Nanophase Materials Sciences at the Oak Ridge National Lab, which is a DOE Office of Science User Facility. The authors would like to thank James Burns for APT sample preparation and running APT experiments. J.X. and C. D. acknowledge the use of computing resources provided by WestGrid and Compute/Calcul Canada.

Appendix A. Supplementary data

Supplementary material related to this article can be found, in the online version, at doi:https://doi.org/10.1016/j.corsci.2020.108749.

References

[1] A. Shukla, A. Pelton, Thermodynamic assessment of the Al-Mn and Mg-Al-Mn systems, J. Phase Equilib. Diff. 30 (1) (2009) 28–39.
[2] N.L. Sukiman, X. Zhou, N. Birbilis, A.E. Hughes, J. Mol, S. Garcia, X. Zhou, G.E. Thompson, Aluminium Alloys - New Trends in Fabrication and Applications, (2012).
[3] M. Zamin, The role of Mn in the corrosion behavior of Al-Mn alloys, CorrosionUs 37 (11) (1981) 627–632.
[4] C.C. Streinz, J.W. Wagner, J. Kruger, P.J. Moran, Analysis of passive film growth by dynamic imaging microellipsometry, J. Electrochem. Soc. 139 (3) (1992) 711–715.
[5] X.X. Yu, A. Gulec, Q. Sherman, K.L. Cwalina, J.R. Scully, J.H. Perepezko, P.W. Voorhees, L.D. Marks, Nonequilibrium solute capture in passivating oxide films, Phys. Rev. Lett. 121 (14) (2018).
[6] Y. Kim, R.G. Buchheit, A characterization of the inhibiting effect of Cu on metastable pitting in dilute Al-Cu solid solution alloys, Electrochim. Acta 52 (7) (2007) 2437–2446.
[7] Y. Kim, R.G. Buchheit, P.G. Kotula, Effect of alloyed Cu on localized corrosion susceptibility of Al-Cu solid solution alloys-Surface characterization by XPS and STEM, Electrochim. Acta 55 (24) (2010) 7367–7375.
[8] F. Sanchette, C. Ducros, A. Billard, C. Rebere, C. Berziou, M. Reffass, J. Creus, Nanostructured aluminium based coatings deposited by electron-beam evaporative PVD, Thin Solid Films 518 (5) (2009) 1575–1580.
[9] D.K. Merl, P. Panjan, I. Milosev, Effect of tungsten content on properties of PVD sputtered Al-W-X alloys, Surf Eng 29 (4) (2013) 281–286.
[10] H. Mraied, W.J. Cai, The effects of Mn concentration on the tribocorrosion resistance of Al-Mn alloys, Wear 380-381 (2017) 191–202.
[11] H. Mraied, W.J. Cai, A.A. Sagues, Corrosion resistance of Al and Al-Mn thin films, Thin Solid Films 615 (2016) 391–401.
[12] J. Creus, C. Berziou, S. Cohendoz, A. Perez, C. Rebere, M. Reffass, S. Touzain, C. Allely, Y. Gachon, C. Heau, F. Sanchette, A. Billard, Reactivity classification in saline solution of magnetron sputtered or EBPVD pure metallic, nitride and Al-based alloy coatings, Corros. Sci. 57 (2012) 162–173.
[13] Z. Szklarska-Smialowska, Pitting corrosion of aluminum, Corros. Sci. 41 (1999) 1743–1767.
[14] S. Gudic, I. Smoljko, M. Kliskic, The effect of small addition of tin and indium on the corrosion behavior of aluminium in chloride solution, J. Alloys. Compd. 505 (1) (2010) 54–63.
[15] E.L. Principe, B.A. Shaw, G.D. Davis, Role of oxide/metal interface in corrosion resistance: Al-W and Al-Mo systems, CorrosionUs 59 (4) (2003) 295–313.
[16] M. Reffass, C. Berziou, C. Rebere, A. Billard, J. Creus, Corrosion behaviour of magnetron-sputtered Al1-x-Mn-x coatings in neutral saline solution, Corros. Sci. 52 (11) (2010) 3615–3623.
[17] J.C. Li, S.H. Nan, Q. Jiang, Study of the electrodeposition of Al-Mn amorphous alloys from molten salts, Surf. Coat. Tech. 106 (2-3) (1998) 135–139.
[18] S.Y. Ruan, C.A. Schuh, Electrodeposited Al-Mn alloys with microcrystalline, nanocrystalline, amorphous and nano-quasicrystalline structures, Acta Mater. 57 (13) (2009) 3810–3822.
[19] G.S. Frankel, R.C. Newman, C.V. Jahnes, M.A. Russak, On the pitting resistance of sputter-deposited aluminum-alloys, J. Electrochem. Soc. 140 (8) (1993) 2192–2197.
[20] T.P. Moffat, G.R. Stafford, D.E. Hall, Pitting corrosion of electrodeposited aluminum-managanese alloys, J. Electrochem. Soc. 140 (10) (1993) 2779–2786.
[21] J.F. Zhang, W. Zhang, C.W. Yan, K.Q. Du, F.H. Wang, Corrosion behaviors of Zn/Al-Mn alloy composite coatings deposited on magnesium alloy AZ31B (Mg-Al-Zn), Electrochim. Acta 55 (2) (2009) 560–571.
[22] G.S. Frankel, Pitting corrosion of metals - A review of the critical factors, J. Electrochem. Soc. 145 (6) (1998) 2186–2198.
[23] A.C. Crossland, G.E. Thompson, C.J.E. Smith, H. Habazaki, K. Shimizu, P. Skeldon, Formation of manganese-rich layers during anodizing of Al-Mn alloys, Corros. Sci. 41 (10) (1999) 2053–2069.
[24] K. Eder, I. McCarroll, A. La Fontaine, J.M. Cairney, Nanoscale analysis of corrosion products: a review of the application of atom probe and complementary microscopy techniques, Jom 70 (9) (2018) 1744–1751.
[25] A. La Fontaine, H.W. Yen, P.J. Felfer, S.P. Ringer, J.M. Cairney, Atom probe study of chromium oxide spinels formed during intergranular corrosion, Scr. Mater. 99 (2015) 1–4.
[26] D. Hudson, G.D.W. Smith, B. Gault, Optimisation of mass ranging for atom probe microanalysis and application to the corrosion processes in Zr alloys, Ultramicroscopy 111 (6) (2011) 480–486.
[27] K. Chernyakova, I. Vrublevsky, V. Klimas, A. Jagminas, Effect of joule heating on formation of porous structure of thin oxalic acid anodic alumina films, J. Electrochem. Soc. 165 (7) (2018) E289–E293.
[28] K. Thompson, D. Lawrence, D.J. Larson, J.D. Olson, T.F. Kelly, B. Gorman, In situ site-specific specimen preparation for atom probe tomography, Ultramicroscopy 107 (2-3) (2007) 131–139.
[29] T.J. Campbell, G. Aral, S. Ogata, R.K. Kalia, A. Nakano, P. Vashishta, Oxidation of aluminum nanoclusters, Phys. Rev. B 71 (20) (2005).
[30] S. Plimpton, Fast parallel algorithms for short-range molecular-dynamics, J. Comput. Phys. 117 (1) (1995) 1–19.
[31] S. Hong, A.C.T. van Duin, Molecular dynamics simulations of the oxidation of aluminum nanoparticles using the ReaxFF reactive force field, J. Phys. Chem. C 119 (31) (2015) 17876–17886.
[32] S. Nose, A unified formulation of the constant temperature molecular-dynamics methods, J. Chem. Phys. 81 (1) (1984) 511–519.
[33] W.G. Hoover, Canonical dynamics - equilibrium phase-space distributions, Phys. Rev. A (Coll Park) 31 (3) (1985) 1695–1697.
[34] A. Stukowski, Visualization and analysis of atomistic simulation data with OVITO-the Open Visualization Tool, Model. Simul. Mat. Sci. Eng. 18 (1) (2010).
[35] Y.L. Huang, H. Shih, H.C. Huang, S. Wu, S. Ramanathan, C. Chang, F. Mansfeld, Evaluation of the corrosion resistance of anodized aluminum 6061 using electrochemical impedance spectroscopy (EIS), Corros. Sci. 50 (12) (2008) 3569–3575.
[36] Y. Zuo, P.H. Zhao, J.M. Zhao, The influences of sealing methods on corrosion behavior of anodized aluminum alloys in NaCl solutions, Surf Coat Tech 166 (2-3) (2003) 237–242.
[37] D.K. Merl, P. Panjan, J. Kovac, Corrosion and surface study of sputtered Al-W coatings with a range of tungsten contents, Corros. Sci. 69 (2013) 359–368.
[38] J.A. Gonzalez, V. Lopez, A. Bautista, E. Otero, X.R. Novoa, Characterization of porous aluminium oxide films from ac impedance measurements, J. Appl. Electrochem. 29 (2) (1999) 229–238.
[39] F. Vurpillot, D. Larson, A. Cerezo, Improvement of multilayer analyses with a three-dimensional atom probe, Surf. Interface Anal. 36 (5-6) (2004) 552–558.
[40] O. Dyck, D.N. Leonard, L.F. Edge, C.A. Jackson, E.J. Pritchett, P.W. Deelman, J.D. Poplawsky, Accurate quantification of Si/SiGe interface profiles via atom probe tomography, Adv. Mater. Interfaces 4 (21) (2017).
[41] J. Chen, W.J. Cai, Effect of scratching frequency on the tribocorrosion resistance of Al-Mn amorphous thin films, Wear 426 (2019) 1457–1465.
[42] B. Zhang, Y. Li, F. Wang, Electrochemical corrosion behaviour of microcrystalline aluminium in acidic solutions, Corros. Sci. 49 (5) (2007) 2071–2082.
[43] J. Zhang, W. Zhang, C. Yan, K. Du, F. Wang, Corrosion behaviors of Zn/Al–Mn alloy composite coatings deposited on magnesium alloy AZ31B (Mg–Al–Zn), Electrochim. Acta 55 (2) (2009) 560–571.
[44] F.J. Martin, G.T. Cheek, W.E. O'Grady, P.M. Natishan, Impedance studies of the passive film on aluminium, Corros. Sci. 47 (12) (2005) 3187–3201.
[45] M.C.L. de Oliveira, V.S.M. Pereira, O.V. Correa, N.B. de Lima, R.A. Antunes, Correlation between the corrosion resistance and the semiconducting properties of the oxide film formed on AZ91D alloy after solution treatment, Corros. Sci. 69 (2013) 311–321.
[46] L. Jinlong, L. Hongyun, Comparison of corrosion properties of passive films formed on phase reversion induced nano/ultrafine-grained 321 stainless steel, Appl. Surf. Sci. 280 (2013) 124–131.
[47] J.A. González, V. López, A. Bautista, E. Otero, X.R. Nóvoa, Characterization of porous aluminium oxide films from a.c. Impedance measurements, J. Appl. Electrochem. 29 (2) (1999) 229–238.
[48] M. Mibus, C. Jensen, X. Hu, C. Knospe, M.L. Reed, G. Zangari, Improving dielectric performance in anodic aluminum oxide via detection and passivation of defect states, Appl. Phys. Lett. 104 (24) (2014).
[49] D.D. Liang, X.S. Wei, C.T. Chang, J.W. Li, Y. Wang, X.M. Wang, J. Shen, Effects of W addition on the electrochemical behaviour and passive film properties of Fe-Based amorphous alloys in acetic acid solution, Acta Metall. Sin.-Engl. 31 (10) (2018) 1098–1108.
[50] J. Amri, T. Souier, B. Malki, B. Baroux, Effect of the final annealing of cold rolled stainless steels sheets on the electronic properties and pit nucleation resistance of passive films, Corros. Sci. 50 (2) (2008) 431–435.
[51] T. Wang, Y.J. Wei, X.X. Chang, C.C. Li, A. Li, S.S. Liu, J.J. Zhang, J.L. Gong, Homogeneous Cu2O p-n junction photocathodes for solar water splitting, Appl Catal B-Environ 226 (2018) 31–37.
[52] D.D. Macdonald, Passivity - the key to our metals-based civilization, Pure Appl. Chem. 71 (6) (1999) 951–978.
[53] K.A. Persson, B. Waldwick, P. Lazic, G. Ceder, Prediction of solid-aqueous equilibria: scheme to combine first-principles calculations of solids with experimental aqueous states, Phys. Rev. B 85 (23) (2012).
[54] A.K. Singh, L. Zhou, A. Shinde, S.K. Suram, J.H. Montoya, D. Winston, J.M. Gregoire, K.A. Persson, Electrochemical stability of metastable materials, Chem. Mater. 29 (23) (2017) 10159–10167.
[55] M. Pourbaix, Atlas of Electrochemical Equilibria in Aqueous Solutions, National Association of Corrosion Engineers, Houston, 1974.
[56] H. Tan, Y.M. Jiang, B. Deng, T. Sun, J.L. Xu, J. Li, Effect of annealing temperature on the pitting corrosion resistance of super duplex stainless steel UNS S32750, Mater. Charact. 60 (9) (2009) 1049–1054.